

# A narrow band graph partitioning method for skin lesion segmentation<sup>☆</sup>

Xiaojing Yuan<sup>a,\*</sup>, Ning Situ<sup>c</sup>, George Zouridakis<sup>a,b,c</sup>

<sup>a</sup>Department of Engineering Technology, University of Houston, Houston, TX 77204, USA

<sup>b</sup>Department of Electrical and Computer Engineering, University of Houston, Houston, TX 77204, USA

<sup>c</sup>Department of Computer Science, University of Houston, Houston, TX 77204, USA

## ARTICLE INFO

### Article history:

Received 15 January 2008

Received in revised form 7 September 2008

Accepted 9 September 2008

### Keywords:

Automatic skin lesion segmentation

Melanoma detection

Border detection

Active contour

Snake

Narrow band energy

## ABSTRACT

Accurate skin lesion segmentation is critical for automated early skin cancer detection and diagnosis. In this paper, we present a novel multi-modal skin lesion segmentation method based on region fusion and narrow band energy graph partitioning. The proposed method can handle challenging characteristics of skin lesions, such as topological changes, weak or false edges, and asymmetry. Extensive testing demonstrated that in this method complex contours are detected correctly while topological changes of evolving curves are managed naturally. The accuracy of the method was quantified using a lesion similarity measure and lesion segmentation error ratio. Our results were validated using a large set of epiluminescence microscopy (ELM) images acquired using cross-polarization ELM and side-transillumination ELM. Our findings demonstrate that the new method can achieve improved robustness and better overall performance compared to other state-of-the-art segmentation methods.

Published by Elsevier Ltd.

## 1. Introduction

Early detection of a cancerous skin lesion is crucial for successful treatment and cure. For example, malignant melanoma, the deadliest form of all skin cancers, has a cure rate of more than 95% if detected at an early stage [1]. To facilitate early detection, several methods have been developed for melanoma detection [2–5]. In all these methods, delineating the skin lesion correctly is key to lesion analysis and accurate diagnosis.

Extracting the lesion area from the background is an essential step in all computer-aided melanoma detection systems and it has attracted continuous research efforts. Thresholding [6–10] and region growing are two simple yet widely used algorithms in the literature. They produce a satisfactory segmentation when skin lesions have clear boundaries. To account for noise and unclear boundaries, several clustering-based methods have been developed that demonstrated improved robustness [10–12]. Another family of popular segmentation methods is based on active contours (or snakes) [13–15], whereby a curve, defined based on partial differential PDEs evolves

toward the local optimum, with respect to an objective function. Typical objective functions are chosen to identify the region of interest and are mostly edge-based or region-based. Chung [16] and Erkol [17] applied edge-based active contours to segment skin lesions. However, leakage occurs at the presence of weak edges and the method is sensitive to the initial conditions. Chan and Vese [18] proposed a region-based active contour method that models non-overlapping homogeneous regions with Gaussian distributions. The method performs well on images with two regions of distinct intensities; however, it presents under-segmentation problems if there are more than two regions of interest in the image. A hierarchical approach has also been proposed [19] to tackle this problem by splitting manually identified subregions.

Following our previous work on region-based object identification [20–22], we developed an active contour-based region-fusion framework. In this approach, a lesion is first segmented into small regions by imposing strict constraints on homogeneity and strong edges on the region-based snakes. Then, these regions are merged based on a centroid distance criterion and gradient information. To improve the performance and computational efficiency of segmentation, a narrow-band graph-partitioning (NBGP) method has been developed.

Experiments and comparison results on more than 200 skin lesion images demonstrate that the proposed algorithm produces segmentation results that are very close to the manual segmentation provided by specialists, even for those images with highly asymmetric lesions, weak and/or false edges, or strong hair and bubble artifacts.

<sup>☆</sup>This work has been supported in part by NSF Grant 521527, the Grants to Enhance and Advance Research program, and the Texas Learning and Computation Center at the University of Houston.

\* Corresponding author.

E-mail addresses: [xyuan@uh.edu](mailto:xyuan@uh.edu) (X. Yuan), [stnstone@gmail.com](mailto:stnstone@gmail.com) (N. Situ), [zouridakis@uh.edu](mailto:zouridakis@uh.edu) (G. Zouridakis).

URL: <http://www.tech.uh.edu/isgrin> (X. Yuan).

The rest of the paper is organized as follows: in Section 2, we present a short review on skin lesion characteristics and image acquisition. In Section 3, we start with an introduction on the level set formulation of the region-based active contours, and then the derivation and development of the NBGP curve evolution for image segmentation is presented in detail. Section 4 describes the new region-fusion algorithm for skin lesion segmentation based on NBGP, whereas Section 5 presents experimental results on more than 200 images from three different imaging modalities. The results obtained with the new method are compared with results from our previously developed methods [10] and from active contours [18,28] and validated against manual segmentation by expert dermatologists. Finally, Section 6 concludes this paper with a discussion on our findings and a summary of future work.

## 2. Characteristics of skin lesion images

In epiluminescence microscopy (ELM), a halogen light is projected into the object rendering the surface translucent [2]. There are two modes of ELM used in clinical applications, oil immersion [23,24] and cross-polarization (XLM) [25]—the latter was developed to reduce light reflection from the epidermis. In side-transillumination ELM (TLM), a bright ring of light positioned around the periphery of a lesion is projected onto the center of the lesion at 45° forming a virtual light source at a focal point about 1cm below the skin surface [26]. Hence, it makes the surface and subsurface of the skin translucent.

Skin lesions appear mostly as dark shades of red color with varying levels of saturation and intensity. They vary in size and shape and their spatial distribution is usually skewed. Figs. 1 and 2 show examples of XLM, TLM and ELM images of malignant and benign skin lesions. Common artifacts and distortions in such images include hair, oil bubbles, and pen marks drawn by dermatologists to indicate the gross lesion location. XLM and ELM images capture mostly surface pigmentation of a skin lesion and usually exhibit well-defined boundaries, whereas TLM images contain information on surface pigmentation and sub-surface blood vasculature around the lesion. Hence, the latter present more challenges in segmentation.

For segmentation purposes, not all vascularization is considered as part of a melanoma. Fig. 3 illustrates a manually segmented TLM

image by a dermatologist. The rationale behind this manual tracing is that the blush outside the contour indicates blood delivered by underlying large vessels that do not directly contribute to the lesion. Inside the contour, angiogenesis occurs at the capillary level, where most of the oxygen exchange takes place, and hence it is considered as part of the lesion. As shown in this figure, there is no clearly defined boundary; instead, the red coloration fades out gradually.

Another challenge in segmentation arises from the lesion area distribution, as most skin lesions are asymmetric. This is an important structural property that dermatologists use for diagnosis but it poses a challenging task in segmentation. The asymmetry property induces significant color and intensity variations within a lesion and this results in false edges, as shown in Fig. 2.

## 3. Curve evolution of region-based and NBGP methods

### 3.1. Level set formulation of region-based curve evolution

Given an image  $I \subset \Omega$ , the region-based active contour model [18] aims to find the curve  $\tilde{C}$  that minimizes the energy-based objective function:

$$E(\tilde{C}) = \lambda_1 \iint_{\text{inside}} |I(x,y) - c_1|^2 dx dy + \lambda_2 \iint_{\text{outside}} |I(x,y) - c_2|^2 dx dy + \mu \mathcal{L}(\tilde{C}) + \nu \mathcal{A}(\text{inside}(\tilde{C})), \quad (1)$$

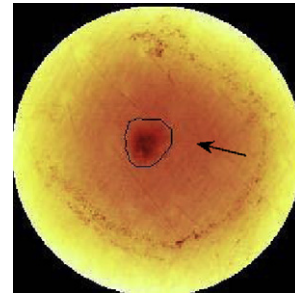


Fig. 3. An example of manual segmentation. The blood in large vessels indicated by the arrow should not be included in the segmented region.

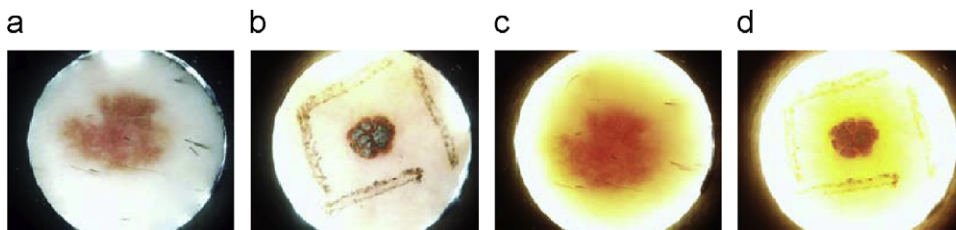


Fig. 1. Examples of XLM and TLM images. (a) and (b) are XLM images of malignant and benign skin lesions, respectively, (c) and (d) are TLM images of malignant and benign skin lesions, respectively.

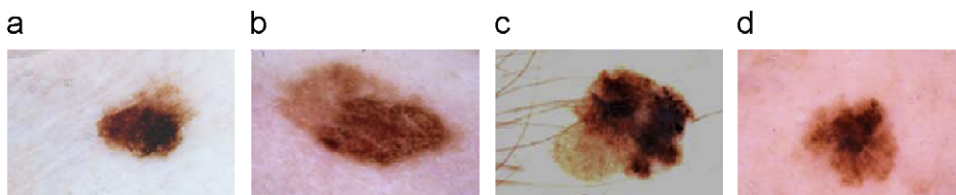


Fig. 2. Examples of ELM images. (a) and (b) are benign lesions, (c) and (d) are malignant lesions.

where  $c_1$  is the average intensity inside  $\tilde{C}$ ;  $c_2$  is the average intensity outside  $\tilde{C}$ ;  $\mu, \nu \geq 0$ ; and  $\lambda_1, \lambda_2 > 0$  are fixed weight defined based on a priori knowledge.  $\mathcal{L}(\tilde{C})$  and  $\mathcal{A}(\tilde{C})$  are two regulation terms. Following Chan's approach [18], we can fix the weights as  $\lambda_1 = \lambda_2 = 1$ ,  $\mu > 0$ , and  $\nu = 0$  loss of generality.

The main drawback of the explicit curve evolution (updating curve  $\tilde{C}$  directly) based on a difference approximation scheme is that topological changes are difficult to handle. The levelset approach [27], on the other hand, handles such changes easily by defining the contour of a region as the zero-level set of a level set function ( $\phi$ ) defined in the whole image region  $\mathfrak{R}$ . Thus, we can represent a plane curve  $\tilde{C}$  as the zero level set of level set function  $\phi(x, y)$ . The relation of a point  $I(x, y)$  to the curve  $\tilde{C}$  and levelset function  $\phi(x, y)$  is given by

$$\begin{cases} I(x, y) \text{ inside } \tilde{C}, & \phi(x, y) > 0 \\ I(x, y) \text{ on } \tilde{C}, & \phi(x, y) = 0 \\ I(x, y) \text{ outside } \tilde{C}, & \phi(x, y) < 0 \end{cases} \quad (2)$$

Given this definition, the level set formulation of Eq. (1) is:

$$\begin{aligned} E(\phi) = & \iint H(\phi(x, y)) |I(x, y) - c_1|^2 dx dy \\ & + \iint (1 - H(\phi(x, y))) |I(x, y) - c_2|^2 dx dy \\ & + \mu \iint |\nabla H(\phi(x, y))| dx dy \end{aligned} \quad (3)$$

where  $H(x)$  is the Heaviside step function.

Calculus of variation was used in [18] to obtain the local minimum of Eq. (3) by solving the following PDE:

$$\frac{\partial \phi}{\partial t} = \delta_\epsilon(\phi) \left( -(I - c_1)^2 + (I - c_2)^2 + \mu \operatorname{div} \left( \frac{\nabla \phi}{|\nabla \phi|} \right) \right) \quad (4)$$

where  $\delta_\epsilon$  is the Dirac function, the derivative of the Heaviside step function in the  $L^2$  space. Solving Eq. (4) using an implicit finite difference scheme [18] gives the update of  $c_1$  and  $c_2$  in each iteration, as shown in Eqs. (5) and (6), respectively:

$$c_1 = \frac{\iint H(\phi(x, y)) I(x, y) dx dy}{\iint H(\phi(x, y)) dx dy} \quad (5)$$

$$c_2 = \frac{\iint (1 - H(\phi(x, y))) I(x, y) dx dy}{\iint (1 - H(\phi(x, y))) dx dy} \quad (6)$$

### 3.2. NBGP curve evolution

The curve evolution for narrow band energy method is as follows. The method updates pixels close to the latest level set contour by optimizing the narrow band energy based on a similarity measure. NBGP was inspired by Sumengen's graph partitioning active contour (GPAC) method [28] and the narrow band energy scheme proposed by Mille and co-workers [29].

While the GPAC method uses a curve evolution scheme to solve the graph partitioning problem, it does not assume any distribution of the image data. Instead, it uses a (dis)similarity measure between a pair of two pixels within the image. The formulation of GPAC defines the same (dis)similarity measure for all regions as follows:

$$\begin{aligned} \min_{\tilde{C}} E1 = & \iint_{R_o} \iint_{R_o} w(p_1, p_2) dp_1 dp_2 + \iint_{R_i} \iint_{R_i} w(p_1, p_2) dp_1 dp_2 \\ & + \mu \oint_{\tilde{C}} ds \end{aligned} \quad (7)$$

where  $R_i$  and  $R_o$  are the image regions inside and outside the curve  $\tilde{C}$ , and  $w(p_1, p_2)$  is a dissimilarity measure between pixels  $p_1$  and  $p_2$ .

As noted by Sumengen [28],

$$\begin{aligned} & \iint_{R_o} \iint_{R_o} w(p_1, p_2) dp_1 dp_2 + \iint_{R_i} \iint_{R_i} w(p_1, p_2) dp_1 dp_2 \\ & + \iint_{R_i} \iint_{R_o} w(p_1, p_2) dp_1 dp_2 = \iint_{\Omega} \iint_{\Omega} w(p_1, p_2) dp_1 dp_2 \end{aligned} \quad (8)$$

where  $\Omega = R_i \cup R_o$ , and the right-hand side of Eq. (8) is constant. Thus, the minimization of the energy  $E1$  in Eq. (7) is equivalent to the following:

$$\min_{\tilde{C}} E2 = - \iint_{R_i} \iint_{R_o} w(p_1, p_2) dp_1 dp_2 + \mu \oint_{\tilde{C}} ds \quad (9)$$

Even though Sumengen formulated and derived the solution based on Eq. (9), the paper points out that incorporating domain knowledge into the (dis)similarity measure is important. However, domain knowledge typically requires a different (dis)similarity measure for different regions within the image. Hence, we extend the formulation of GPAC by not only allowing different (dis)similarity measures on distinct regions, but also different non-negative weights assigned to each measure (Eq. (10)). Although an efficient implementation of GPAC has been proposed [28], it is still not efficient on high resolution images. Here we propose to use narrow band energy in GPAC instead of computing energy over the whole image. This is inspired from Mille and co-worker [29]'s experiment showing that using narrow band energy can improve efficiency on their curve evolution scheme. Our narrow band graph partitioning objective function is formulated as follows:

$$\begin{aligned} \min_{\tilde{C}} E = & \lambda_1 \iint_{R_o} \iint_{R_o} w_1(p_1, p_2) dp_1 dp_2 \\ & + \lambda_2 \iint_{R_i} \iint_{R_i} w_2(p_1, p_2) dp_1 dp_2 \\ & + \lambda_3 \iint_{R_i} \iint_{R_o} w_3(p_1, p_2) dp_1 dp_2 + \mu \oint_{\tilde{C}} ds \end{aligned} \quad (10)$$

where the *inward* narrow band region  $R_i$  is bounded by curve  $\tilde{C}$  and  $\tilde{C} - b_i \tilde{N}$ , where  $\tilde{N}$  is the outward unit normal of curve  $\tilde{C}$ . Similarly, the *outward* narrow band region  $R_o$  is bounded by curve  $\tilde{C}$  and  $\tilde{C} + b_o \tilde{N}$ . Here,  $b_i$  and  $b_o$  are fixed parameters that determine the size of the inward and outward narrow band, and  $\lambda_k (k = 1, 2, 3)$  are non-negative weights for each (dis)similarity measure. In the first two terms,  $w_k (k = 1, 2)$  are dissimilarity measures for two points,  $p_1$  and  $p_2$ , either both in the outward narrow band region ( $w_1(p_1, p_2)$ ) or both in the inward narrow band region ( $w_2(p_1, p_2)$ ). In the third term,  $w_3$  is a similarity measure for two points,  $p_1$  and  $p_2$ , each in the outward or inward narrow band ( $w_3(p_1, p_2)$ ). The solutions will be derived based on this generalized energy function.

The regions  $R_i$  and  $R_o$  defined by the current curve  $\tilde{C}$  in the energy function of Eq. (10) are mostly homogeneous within, and have maximum difference between, two regions. Unlike the cost function defined in Ref. [28], the sum of the first three terms depends on the curve, the (dis)similarity measures ( $w_k$ ), and the parameter ( $\lambda_k$ ) chosen, which will not always be constant. Thus, we cannot substitute any of them with the other.

#### 3.2.1. Variational scheme for narrow band region energy

The curve evolution scheme that minimizes the energy function in Eq. (10) is based on gradient descent optimization. Let  $M_1$  denote the first term of Eq. (10), i.e.,  $M_1 = \iint_{R_o} \iint_{R_o} w_1(p_1, p_2) dp_1 dp_2$ . Note that the similarity measure  $w_1$  is not changing with respect to  $t$ . Following the gradient descent method, the derivative of  $M_1$  with

respect to time  $t$ , it can be derived as follows:

$$\frac{\partial M_1}{\partial t} = \oint_{\bar{C}_{ob}} \langle \bar{C}'(t), G_1 \bar{N} \rangle ds + \iint_{R_o(\bar{C})} \frac{\partial}{\partial t} G_1(X, t) dX \quad (11)$$

where  $\bar{C}_{ob}$  is the boundary curve of region  $R_o$ , which consists of the curve  $\bar{C}$  and the curve  $\bar{C} + b_o \bar{N}$ .  $\bar{C}'(t)$  denotes the first derivative of curve  $\bar{C}$ . The term  $G_1(X, t)$  here is defined as  $G_1(X, t) = \iint_{R_o(\bar{C})} w_1(X, Y) dY$ . The first term of Eq. (11) can be further decomposed as

$$\oint_{\bar{C}_{ob}} \langle \bar{C}'(t), G_1 \bar{N} \rangle ds = \oint_{\bar{C}} \langle \bar{C}'(t), G_1 \bar{N} \rangle ds - \oint_{\bar{C}} \langle \bar{C}, G_1 \bar{N} \rangle ds \quad (12)$$

where  $\bar{C}_o$  denotes the outer bound curve  $\bar{C} + b_o \bar{N}$ .

Based on the Frenet equation for a planar curve, we know that  $d\bar{N}_i/ds = -\kappa \bar{T}$ , in which  $\bar{N}_i$  is the inward unit normal vector,  $\bar{T}$  is the unit tangent vector, and  $\kappa$  is the curvature. Since the magnitude of both  $\bar{N}_i$  and  $\bar{T}$  is unity,  $|d(\bar{C} + b_o \bar{N})/ds| = |\bar{T}(1 + b_o \kappa)| = |1 + b_o \kappa|$ . Furthermore,  $\langle b_o \bar{N}_t, G_{1+} \bar{N} \rangle = b_o G_{1+} \langle \bar{N}_t, \bar{N} \rangle = b_o G_{1+}/2 \cdot (\bar{N}^2)_t = b_o G_{1+}/2 \cdot 1_t = 0$ , where  $G_{1+}$  means that the point  $X$  in  $G_1(X, t)$  is on the curve  $\bar{C} + b_o \bar{N}$ . Thus, the first term of Eq. (12) can be written as

$$\begin{aligned} \oint_{\bar{C}_o} \langle \bar{C}'(t), G_1 \bar{N} \rangle ds &= \oint_{\bar{C}} \langle (\bar{C} + b_o \bar{N})'(t), G_{1+} \bar{N} \rangle \left| \frac{d(\bar{C} + b_o \bar{N})}{ds} \right| ds \\ &= \oint_{\bar{C}} \langle (\bar{C} + b_o \bar{N})'(t), G_{1+} \bar{N} \rangle |1 + \kappa b_o| ds \\ &= \oint_{\bar{C}} \langle \bar{C}'(t), |1 + \kappa b_o| G_{1+} \bar{N} \rangle ds \end{aligned} \quad (13)$$

The second term in Eq. (11) can be obtained by following the same procedure as above, but replacing  $G_1(X, t)$  with  $w_1(p_1, p_2)$ , as follows:

$$\begin{aligned} \iint_{R_o(\bar{C})} \frac{\partial}{\partial t} G_1(X, t) dX &= \iint_{R_o(\bar{C})} \oint_{\bar{C}} \langle \bar{C}'(t), (-w_1(p, \bar{C}) \\ &\quad + |1 + \kappa b_o| w_1(p, \bar{C} + b_o \bar{N})) \bar{N} \rangle ds dp \end{aligned} \quad (14)$$

Substituting Eqs. (13) and (14) into Eq. (11), we get

$$\begin{aligned} \frac{\partial M_1}{\partial t} &= 2 \oint_{\bar{C}} \left\langle \bar{C}'(t), \left( \iint_{R_o(\bar{C})} (-w_1(p, \bar{C}) \right. \right. \\ &\quad \left. \left. + |1 + \kappa b_o| w_1(p, \bar{C} + b_o \bar{N})) dp \right) \bar{N} \right\rangle ds \end{aligned} \quad (15)$$

Similarly to the definition of  $M_1$  and  $G_1$ , we can define  $M_2, G_2$ , and  $M_3, G_3$  for the second and third terms of Eq. (10), respectively. Following the same procedure as above, we can derive the derivatives of the second ( $M_2$ ) and third terms ( $M_3$ ) in Eq. (10) with respect to  $t$ .

$$\begin{aligned} \frac{\partial M_2}{\partial t} &= 2 \oint_{\bar{C}} \left\langle \bar{C}'(t), \left( \iint_{R_i(\bar{C})} w_2(p, \bar{C}) \right. \right. \\ &\quad \left. \left. - |1 - \kappa b_i| w_2(p, \bar{C} - b_i \bar{N}) dp \right) \bar{N} \right\rangle ds \end{aligned} \quad (16)$$

and

$$\begin{aligned} \frac{\partial M_3}{\partial t} &= \oint_{\bar{C}} \left\langle \bar{C}'(t), \left( \iint_{R_o(\bar{C})} w_3(p, \bar{C}) - |1 - \kappa b_i| w_3(p, \bar{C} - b_i \bar{N}) dp \right. \right. \\ &\quad \left. \left. + \iint_{R_i(\bar{C})} |1 + \kappa b_i| w_3(p, \bar{C} + b_o \bar{N}) - w_3(p, \bar{C}) dp \right) \bar{N} \right\rangle ds \end{aligned} \quad (17)$$

### 3.2.2. Levelset formulation of narrow band graph partitioning

Combining Eqs. (15)–(17), and the curvature flow that minimizes the regulation term  $\mu \oint_{\bar{C}} ds$  in the energy function equation (10), we can obtain the curve evolution scheme by letting the derivative of the energy  $E$  in Eq. (10) with respect to  $t$  to be 0. Using the level set formulation, we convert the explicit curve evolution scheme into an explicit solution, assuming that  $\phi(x, y)$  is a signed distance function for curve  $\bar{C}$  in the Lipchitz space as defined in Eq. (2). Similarly to the formulation of other region-based active contours, the levelset evolution equation to minimize Eq. (10) is the following PDE:

$$\frac{\partial \phi}{\partial t} = (A_i + A_o + \mu \kappa) |\nabla \phi| \quad (18)$$

where

$$\begin{aligned} A_i &= \iint_{R_i(x, y)} -2|1 - \kappa b_i| w_2(p, (x, y) - b_i \bar{N}) \\ &\quad + 2w_2(p, (x, y)) - w_3(p, (x, y)) + |1 + \kappa b_o| w_3(p, (x, y) + b_o \bar{N}) dp \end{aligned}$$

and

$$\begin{aligned} A_o &= \iint_{R_o(x, y)} -|1 - \kappa b_i| w_3(p, (x, y) - b_i \bar{N}) \\ &\quad + w_3(p, (x, y)) - 2w_1(p, (x, y)) \\ &\quad + 2|1 + \kappa b_o| w_1(p, (x, y) + b_o \bar{N}) dp \end{aligned} \quad (20)$$

The curve evolves based on the narrow band energy of regions  $R_i(x, y)$  and  $R_o(x, y)$  defined by  $\kappa b_i$  and  $\kappa b_o$ , while  $p$  denotes a pixel within the regions  $R_i(x, y)$  or  $R_o(x, y)$ , which are defined by the signed distance function  $\phi(x, y)$  as follows:

$$R_i(x, y) = \{(u, v) | -b_i \leq \phi(u, v) - \phi(x, y) \leq 0\} \quad (21)$$

$$R_o(x, y) = \{(u, v) | 0 \leq \phi(u, v) - \phi(x, y) \leq b_o\} \quad (22)$$

## 4. Skin lesion segmentation algorithm based on region fusion of narrow band graph partitioning

In this section, we describe in detail a two-stage framework that integrates region fusion and narrow band graph partitioning (NBGP) active contour. The resulting skin lesion segmentation algorithm can efficiently and effectively segment challenging images as outlined in Section 2.

### 4.1. Region-fusion-based segmentation

As mentioned in Section 1, the Chan–Vese model [18] was developed for segmentation of bi-modal images. If there are more than two homogenous regions in the image, the method will under-segment the image. A hierarchical approach [19] was used to continue segmenting subregions requiring further segmentation. The hierarchical approach can only handle non-overlapping regions and expert interaction is needed after each iteration to decide which region needs to be segmented further.

In contrast, the proposed region-fusion-based segmentation framework can automate the whole process. The image is first segmented into small regions using Chan–Vese model with strict constraints on homogeneity and strong edge. Then small regions that belong to the same homogeneous cluster are merged together based on centroid intensity and gradient information. The following Algorithm 1 summarizes the hierarchical region fusion framework.



**Algorithm 1.** Region fusion framework scheme

**Input:** The preprocessed image  $\Omega_0$   
**Output:** The segmentation result  $\Omega_R$

```

1  $i = 0$ ;
  /* Stage 1: Iterative Segmentation; */
2 while (1) do
3   Apply a bi-mode segmentation method, i.e. Chan-Vese model, on  $\Omega_i$ ;
4   The output is the boundary  $\partial\Omega_{i+1}$  and its enclosed region  $\Omega_{i+1}$ ;
5    $i = i + 1$ ;
6   if  $\text{area}(\Omega_{i+1})/\text{area}(\Omega_0) \leq \text{MinArea}$  or  $i = \text{MaxNum}$  then
7     BREAK;
8   end
9 end
  /* Stage 2: Region Merging; */
10 while (1) do
11   if  $i = 1$  then
12      $\Omega_R = \Omega_1$ ;
13     BREAK;
14   end
15   if  $\text{NOT}(\text{TESTMERGE}(\Omega_i, \Omega_{i-1}))$  then
16      $\Omega_R = \Omega_i$ ;
17     BREAK;
18   else
19      $\text{MERGE}(\Omega_i, \Omega_{i-1})$ ;
20      $i = i - 1$ ;
21   end
22 end
23  $\Omega_R$  is the segmented region;

```

At the first stage, active contours are applied iteratively inside each segmented region. Based on prior knowledge of the specific application, different strategies can be chosen to further segment only regions with lower intensity, higher intensity, or both. In skin lesion segmentation, since the skin lesion always has lower intensity than the healthy skin and blood vasculature, we always segment regions with lower intensity further. The iterative segmentation procedure stops when the number of pixels inside the region is smaller than  $\text{MinArea}\%$  of the total number of pixels in the image. For skin lesion segmentation, after extensive testing, we found that  $\text{MinArea} = 10$  guarantees that small lesions are correctly segmented, while avoiding the problem of oversegmentation.

The second stage merges overlapping and/or non-overlapping regions based on two criteria [ $\text{Testmerge}()$ ]. The centroid criterion computes the absolute difference of the intensity centroid of adjacent regions  $\Omega_{i-1} - \Omega_i$  and  $\Omega_i$  (notice that  $\Omega_i \subseteq \Omega_{i-1}$ ), and merges the regions together if its value falls below a threshold  $\tau$ . Edge strength is defined as the average gradient magnitude of pixels inside a dilated boundary, the same as used in the scoring system of Ref. [10]. If the edge strength of the inside region  $\Omega_{i-1}$  is greater than that of the outside region  $\Omega_{i-1}$ , then the two regions are merged together. The area with higher edge strength is preferred based on this gradient criterion.

Fig. 4 shows examples of how the two criteria work successfully when large blood vessels are not present (the first two lesion images) and when they are present (the last two lesion images). The large blood vessels are included in the red boundary when we apply the Chan-Vese model one time.

**4.2. Narrow band graph partitioning image segmentation algorithm**

Algorithm 2 summarizes the narrow band graph partitioning active contour for image segmentation. As pointed out in Ref. [19],

only a rough estimation is required to direct the curve evolution. The estimation procedure can make the algorithm faster by reducing the amount of time required to solve the PDE. In our algorithm, the curve evolution is further sped up by evolving over a relatively small ring (Narrow Band) for both the level set function update and the region-based energy similarity measure. We denote the narrow band size for levelset function update as  $ubs$ . Pixels inside this band belong to *ActivePixels*. For the region-based similarity measure, we assume that the inward and outward narrow band has the same size, denoted as  $ebs$ . In Algorithm 2, we use the simplified level set solution (from Eqs. (19) and (20)) for curve evolution Eq. (18) as detailed below. Assuming the narrow band size is small and the curve is sufficiently smooth, then  $b_i\kappa$  and  $b_o\kappa$  will approach zero. Thus, the equations for  $A_i$  and  $A_o$  can be simplified as follows:

$$A_i = \iint_{R_i(x,y)} -2w_2(p, (x,y) - b_i\vec{N}) + 2w_2(p, (x,y)) - w_3(p, (x,y)) + w_3(p, (x,y) + b_o\vec{N}) dp \quad (23)$$

and

$$A_o = \iint_{R_o(x,y)} -w_3(p, (x,y) + b_o\vec{N}) + w_3(p, (x,y)) - w_1(p, (x,y)) + 2w_1(p, (x,y) + b_o\vec{N}) dp \quad (24)$$

Essentially, this is equal to treating the arc-length element  $|(\vec{d}\vec{C} + b_o\vec{N})/ds|$  and  $|(\vec{d}\vec{C} - b_i\vec{N})/ds|$  as constants whose values are 1. The same approximate scheme has also been used in Ref. [29].

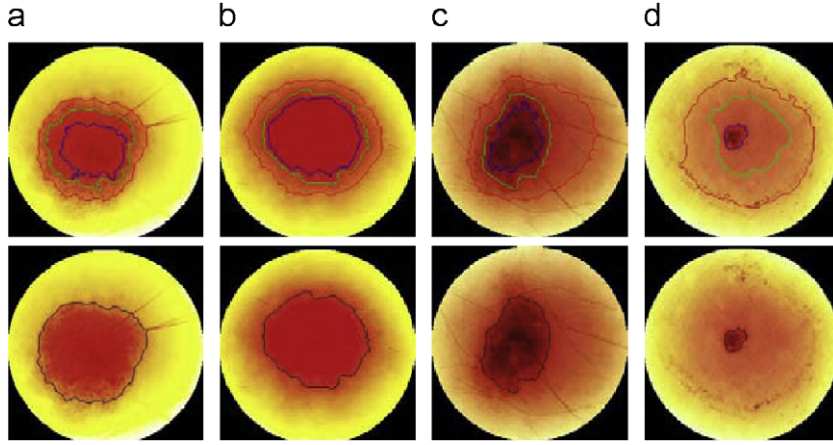


**Fig. 4.** TLM image segmentation examples. Top row: results from the hierarchical region fusion algorithm using the Chan–Vese active contour. The red, blue, and green boundaries represent results after the first three iterations, respectively. Bottom row: final result. The error ratio (see Eq. (26)) for each image is shown in the third row. (a) 7.91%; (b) 4.71%; (c) 6.89% and (d) 36.19%.

#### Algorithm 2. Narrow band graph partitioning active contour

**Input:** InitialCurve  $\bar{C}$ , MaxIterNum  
**Output:** Final level set function  $\phi$  and the corresponding curve

```

1 iter ← 0;
2 while iter ≤ MaxIterNum do
3   ActivePixels = REINITIALIZE( $\phi$ );
4   forall  $(x, y) \in \text{ActivePixels}$  do
5     UPDATE ( $\phi(x, y)$ ) by Eq. (18);
6   end
7   EXTRACTCURRENTCURVE();
8   if CONVERGE then
9     BREAK;
10  end
11  iter = iter + 1;
12 end
13 OUTPUTLATESTCURVE();

```

The three steps in Algorithm 2 are described in detail below.

**Input:** The input of the algorithm, such as InitialCurve  $\bar{C}$ , MaxIterNum,  $ebs$ , and  $ubs$  is provided by the user.

**Step A. Reinitialization procedure:** First, the level set function of each pixel is reinitialized locally [Reinitialize( $\phi$ )] to a signed distance function. To reduce the computational cost, we adopted the approximation scheme presented in Ref. [28]. Instead of using an exact sign distance function as the level set function  $\phi$ , we approximate it within  $(ebs + ubs)$  layers of pixels. The zeroth layer is the current curve on which all level set functions are zero. The four-connected neighbors in both directions of the pixels on the curve (i.e., in the zeroth layer) constitute the first layer. The second layer consists of the four-connected neighbors of the first layer pixels that do not belong in the zeroth layer. The procedure continues until the  $(ebs + ubs)$ th layer is formed. All pixels of these  $(ebs + ubs)$ th layers are selected as *ActivePixels*. Then the layer number for all pixels inside the current curve will be multiplied by  $-1$  to indicate that they are inside the region.

**Step B. Curve updating:** Each pixel within the *ActivePixels* is then examined and its level set function is updated [Update( $\phi(i, j)$ )] according to Eq. (18). The upwind scheme proposed in Ref. [27] is used to calculate  $|\nabla \phi|$ . For a pixel  $(x, y)$ , we need to know the feature of the point  $((x, y) + b(\bar{N}))$  in Eq. (24). This feature (such as intensity) is approximated by the feature of the closest point to  $(x, y)$  on layer  $b$ . If more than one point is found, their average similarity measure will be used to update the function. A similar procedure is used for the

term  $((x, y) - b(\bar{N}))$  in Eq. (23). After the levelset functions for all the *ActivePixels* are updated, the current curve is extracted within the narrow band by considering the zero level set crossings [ExtractCurrentCurve()].

**Step C. Convergence control:** If a certain number of iterations is reached (MaxIterNum) or the curve does not move [Converge] within two iterations, then the curve evolution is completed and the final curve is extracted [OutputLatestCurve()]. Otherwise, Step B is repeated.

#### 4.3. Computational and space complexity analysis

In order to reduce the computational cost, several techniques are employed. First of all, a fast implementation of active contours [30] is used for all curve evolution. As described in detail in Section 3, instead of solving the objective function defined in Eq. (1) directly at each iteration, the sign of a levelset function  $\phi(x, y)$  on a pixel  $p(x, y)$  is used to indicate the changes. This is sufficient for segmentation purpose. When the objective function decreases, the sign of  $\phi(x, y)$  on  $p(x, y)$  changes; otherwise, it remains the same as in the last iteration. The discrete form of the spatial constraint, i.e., the length term in Eq. (3), used in our experiment is shown in Eq. (25) which is the same as that in Ref. [30].

$$\nabla H(\phi(x, y)) = ((H(\phi(x + 1, y)) - H(\phi(x, y))), (H(\phi(x, y + 1)) - H(\phi(x, y)))) \quad (25)$$

The time complexity of the level set-based curve evolution was proven [30] to be  $O(M \times N)$ , where  $M \times N$  is the total number of pixels of the image.

Secondly, while updating the levelset function, we adopted the narrow band approach initially proposed in Ref. [31] and extensively analyzed and optimized in Ref. [32]. The idea is to consider only the pixels close to the current contour (i.e., *ActivePixels*). To reduce the cost of updating the narrow band itself from iteration to iteration, the contour position and the set of narrow band pixels are updated only in cases where the contour is very close to the borders of the current band. A significant cost reduction can be achieved through this approach [33].

In order to further reduce the computational cost and improve the convergence speed, a multiscale technique is used and combined with our NBGP curve evolution. Specifically, a Gaussian pyramid [34] of images is built upon the full resolution image, and similar narrow band active contour problems are defined across the different granularity levels. Usually, this technique is applied to a pyramid with

two or three levels. The first level is the scale with a size smaller than  $128 \times 128$ . A Chan–Vese model is used on the first level to obtain an initial curve for NBP, and then the NBP (Algorithm 2) is applied. The boundary obtained on the coarser scale is used as the initial curve for the next finer scale. Only the first three scales are used. Then, the boundary obtained at the third level is used as the initial curve on the original image scale.

We performed the iteration on the coarser scale first, and then applied the result as the initial curve on finer scale. This approach can increase the speed because one iteration on a coarser scale saves several iterations on a finer scale. Details of parameter setting for our pyramid method are described in Section 5.2.

Considering all these mechanisms, the computational complexity of our segmentation algorithm is analyzed here. For a skin lesion image with dimensions  $N \times N$ , we can assume that the number of pixels on the boundary of the lesion is on the order of  $O(N)$  considering the common shape of a lesion. Then the number of *ActivePixels* is  $2 \times \text{ubs} \times N$ . For each pixel in *ActivePixels*, the total number of pixels in an outward and inward narrow band region is  $2 \times \text{ebs} \times N$ . Thus, the computational complexity of the for loop in Algorithm 2 to update the level set function  $\phi$  is  $O(4 \times \text{ebs} \times \text{ubs} \times N^2)$ . For small  $\text{ebs}$  and  $\text{ubs}$ , such that  $\text{ebs}/N < 0.1$  and  $\text{ubs} \leq 2$ , the computational complexity is  $O(N^2)$  in each iteration.

For the re-initialization function,  $\text{Reinitialize}(\phi)$ , in Algorithm 2, we assign the layer number to pixels based on four-connected neighbors. The number of pixels inside the  $(\text{ebs} + \text{ubs})$  layer is  $2 \times (\text{ebs} + \text{ubs}) \times N$ . For small  $(\text{ebs} + \text{ubs})$ , the computational complexity of function  $\text{Reinitialize}(\phi)$  is  $O(N)$ .

The overall computational complexity of our skin lesion segmentation algorithm is  $O(N^2)$  in each iteration when the image size is  $N \times N$ , linearly related to the  $\text{MaxIterNum} \times \text{LevelNum}$ , in which  $\text{MaxIterNum}$  is the maximum iteration number of the curve evolution NBP algorithm, and the  $\text{LevelNum}$  is the number of multiple scale used in the Gaussian pyramid. This is much better than the computational complexity of  $O(N^3)$  (under the same assumption that the number of pixels on the boundary of a skin lesion is  $O(N)$ ) in each iteration for image segmentation based on graph partitioning active contour (GPAC) [28].

For skin lesion image segmentation, when using a 64bit AMD machine with 2.4GHz Opteron processors and 2GB RAM, the run-time of NBP ranges from 104 s (for image size  $577 \times 397$ ) to 923 s (for image size  $2465 \times 1637$ ). Our program was implemented in MATLAB® Version 7.1 (R14SP3).

## 5. Experiments and evaluation

### 5.1. Image acquisition

Our XLM and TLM images were acquired with a Nevoscope [35,36] that uses a  $5 \times$  optical lens (manufactured by Nikon, Japan). An Olympus C2500 digital camera was attached to this Nevoscope. Fifty one XLM images and 60 TLM images were used in our experiments. The image resolution is  $1712 \times 1368$  pixels. A region of interests (ROI), identified in every image, was segmented, manually by dermatologists and automatically using our method. This step was performed on a  $236 \times 236$  region obtained from a preprocessing step described in the next Section. Results from manual segmentation was used as reference for method evaluation.

In addition, one hundred ELM images were acquired using an oil immersion technique [37,38]. Among them, thirty images were melanoma and the rest were benign. Three dermatologists performed segmentation on the original image scale. The average contour was used as reference in our experiments.

**Table 1**

Parameters used in our experiments

Image	MA	RF	TS	IT	$\mu$	ebs	ubs	$\lambda_1$	$\lambda_2$	$\lambda_3$
XLM	No	No	0.1	10	255	10	1	1.5	0.5	0.5
TLM	No	Yes	0.1	10	255	10	1	1.5	0.5	0.5
ELM	Yes	No	0.1	10	255	10	Coarse scale: 2 Fine scale: 1	5 5	0 0.5	1 1

MA: Multi-scale approach. RF: Region fusion approach. TS: Time step. IT: Maximum number of iteration.

### 5.2. Pre-processing and parameter settings

The same pre-processing procedures described below for XLM, TLM, and ELM images are used to pre-process the same type of skin lesion images before any segmentation methods are applied on them. This is to make sure that the comparisons among the proposed method, the Chan–Vese model, the GPAC [28] approach, and our previously developed algorithms [10] are fair.

To reduce the computational cost without sacrificing the quality of the segmentation results, TLM and XLM images were resized to a  $256 \times 256$ . During image acquisition, an extra effort was made so that the lesion appeared close to the center of the images. To find appropriate ROIs, a Canny edge detector was applied to extract the boundaries of peripheral dark areas. The center of a rectangular ROI was identified by a Hough transform. The ROI was then bounded by circular boundary defined earlier with size  $236 \times 236$ . A median filter and a Gaussian filter were applied to smooth the image and to reduce noise. In our experiments, filter size was  $5 \times 5$  and the standard deviation for the Gaussian filter was 1.5. The same preprocessing steps were used in [10].

For the curve evolution, we adopted the same similarity measure employed in [28], and used its negative as the dissimilarity measure:  $w_1(p_1, p_2) = w_2(p_1, p_2) = -w_3(p_1, p_2) = |I(p_1) - I(p_2)|$ , where  $I(p)$  is the intensity of pixel  $p$ . The selection of  $\lambda_i$  in Eq. (10) is based on domain knowledge that healthy skin outside the lesion is typically homogenous while skin inside the lesion is more heterogeneous. As shown in Table 1,  $\lambda_1$  is chosen to be higher than  $\lambda_2$  in our experiments, placing more emphasis on the outside region than on the inside. This makes sure that a larger heterogeneous region will be segmented that includes any angiogenesis that might occur at the capillary level. Besides the intensity value, other computationally intensive features, such as color and texture, can also be used to define the energy function, but is out of the scope of this paper.

Table 1 summarizes our experimental parameters. Initialization of Chan–Vese model was randomly generated close to the center of an image within a  $10 \times 10$  square for XLM images or in a  $40 \times 40$  square for the TLM images. The rationale for this particular parameter selection for XLM and TLM images is that it encourages homogeneity of the outward narrow band rather than the inward one, since skin lesions usually vary in intensity distribution while healthy skin appears more uniform. In both imaging modalities, results from the Chan–Vese model served as the initial curve for NBP and GPAC in our experiments to provide a good guess and therefore to improve the convergence speed.

The size of ELM images varied from  $577 \times 397$  to  $2465 \times 1637$ . Hence, we used the original image without resizing in our experiments. To compensate for size-induced computational cost, a multi-scale Gaussian pyramid was employed. We used three levels for lesion segmentation, in which the third level was the original image. The first level was the scale with image resolution reduced to less than  $128 \times 128$ . The Chan–Vese model was used on this level to obtain an initial curve before the NBP or GPAC was applied. To smooth the images on all scales, median filtering with a size of 8, 16, and 20, as well as a  $5 \times 5$  Gaussian filter with a standard deviation of 1.5 was applied to all scales. The boundary obtained through



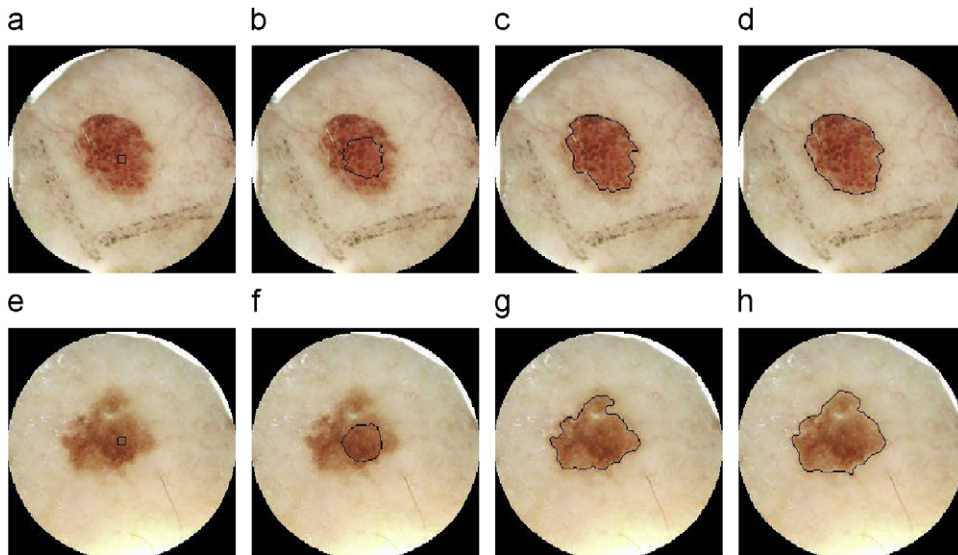


**Fig. 5.** Segmentation of two XLM images. First example: (a)–(d). Second example: (e)–(h). (a) Initial curve. (b) Curve after 10 iterations. (c) Result of Chan-Vese's method. (d) Result of our method. (e) Initial curve. (f) Curve after 10 iterations. (g) Result of Chan-Vese's method. (h) Result of our method.

Algorithm 2 on the coarse scale was used as the initial curve on the finer level. Table 1 shows the parameters used for ELM images. The rationale for this particular parameter selection for the coarser scales (the first and second scales) was to ensure homogeneity in the outward band of the boundary while allowing the inward band to include inhomogeneous structures. At the third level, we chose parameters to avoid misleading boundary evolutions due to noisy pixels and structures (very small regions of irregularity) on the background healthy skin. A small number of iterations (10) was needed in all scales for all images, since we used Chan-Vese model as the initial curve in the coarsest scale, and this provided good guesses. As the result, only a small number of iteration was needed to converge to the best skin lesion boundary. This approach gave good segmentation results within a reasonable amount of time.

### 5.3. Performance analysis

We adopted the quantitative metrics used in Ref. [10] for performance evaluation. The error rate  $E$  is defined as the normalized agreement of segmentation results and the reference. Let  $c$  denote the contour of the segmented area,  $c_r$  the reference contour,  $\mathcal{A}(c)$  the set of pixels enclosed by contour  $c$ ,  $|C|$  the cardinality of set  $C$ , and  $\oplus$  the Exclusive OR logical operation. The error rate is defined as follows:

$$E = \frac{|\mathcal{A}(c) \oplus \mathcal{A}(c_r)|}{|\mathcal{A}(c)| + |\mathcal{A}(c_r)|} \quad (26)$$

We also adopted a similarity metric from Ref. [39] as follows:

$$S = \frac{2 \times |\mathcal{A}(c) \cap \mathcal{A}(c_r)|}{|\mathcal{A}(c)| + |\mathcal{A}(c_r)|} \quad (27)$$

It is obvious that  $E + S = 1$ .

Fig. 5 illustrates segmentation results from two XLM images. The proposed method demonstrated significant improvements in error rate. In the first case (top row), the error rates for our method and Chan-Vese's method are 4.3% and 12.26%, respectively. In the second case (bottom row), the error rates for our method and Chan-Vese's method are 5.34% and 10.69%, respectively.

Fig. 6 illustrates segmentation of two TLM images. In the first example (top row), both methods segmented the large lesion successfully with low error rate. Ours and Chan-Vese's methods achieved

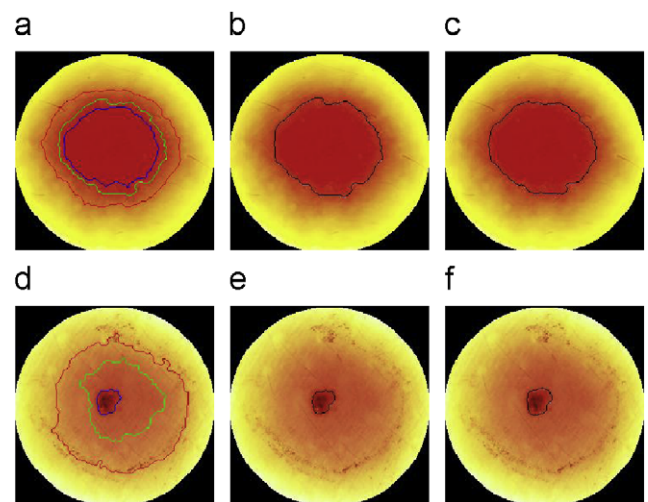


**Fig. 6.** Segmentation of two TLM images. (a) Segmentation with Chan-Vese's method. (b) Region fusion of Chan-Vese's method. (c) Result of our method. (d) Segmentation with Chan-Vese's method. (e) Region fusion of Chan-Vese's method. (f) Result of our method.

**Table 2**

Average segmentation error rates (%) and their standard deviation

Error (Std)	NBGP	CV	GPAC	SS	PS	SPCT	FC
XLM	<b>12.41</b> (±10.2)	13.7 (±8.5)	12.88 (±9.1)	15.15 (±15.2)	18.88 (±12.6)	16.57 (±14.8)	15.22 (±15.4)
TLM	<b>12.28</b> (±8.5)	12.67 (±9.0)	15.93 (±10.8)	14.08 (±13.9)	23.09 (±22.1)	19.22 (±18.0)	16.57 (±18.3)

NBGP: our method. CV: Chan-Vese's method. GPAC: SS: Scoring system. PS: Principal component transform (PCT) method for XLM and Sigmoid-based thresholding for TLM. SPCT: Sigmoid-based PCT method. FC: Fuzzy C-Mean.

error rates at 5.47% and 5.18%, respectively. In the second example (bottom row), our method demonstrated improved accuracy over a small lesion with an error rate of 23.36%; whereas the error rate of Chan-Vese's method was 30.52%.

We performed a comparison study with methods presented in Refs. [10,18,28] and summarize the average error rate in Table 2. The image set consisted of 51 XLM images and 60 TLM images. In both



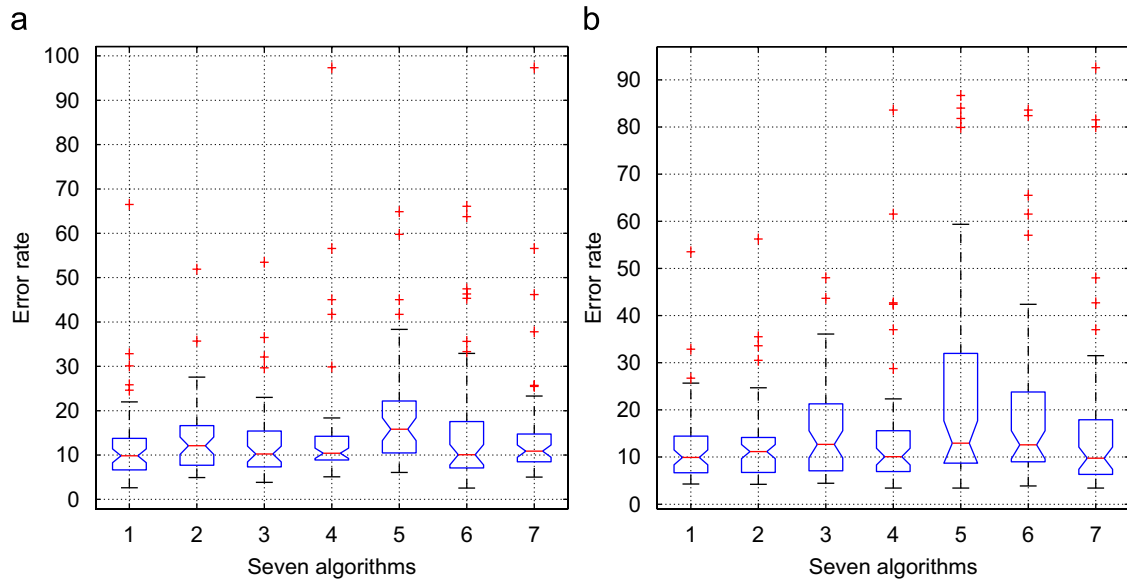


**Fig. 7.** Error ratio of six segmentation methods. The x-axis denotes the methods as follows: 1: Our method (NBGP). 2: Chan-Vese's method. 3: GPAC. 4: Scoring system. 5: Principal component transform (PCT) method for XLM and Sigmoid-based thresholding for TLM. 6: Sigmoid-based PCT method. 7: Fuzzy C-Mean. Methods 4–7 are from Ref. [10]. (a) Shows error ratios of XLM images. (b) Shows error ratios of TLM images.

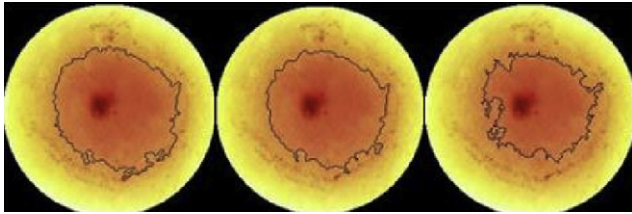


**Fig. 8.** Incorrect lesion segmentation. The methods that generate these results are, from left to right: Sigmoid based thresholding, PCT+Sigmoid, and Fuzzy C-mean.

imaging modalities, our method exhibits significantly improved performance. As shown in box plot (Fig. 7), the new method demonstrated smaller variance and provided the best results in average error ratio, and the first quarter, the median, and the third quarter of the distribution. Although the lowest error ratio in both cases was achieved by other methods, our method was consistent and significantly accurate on average.

Our understanding of the improved performance of our method is twofold: First, the  $\mu \times \mathcal{L}$  term in Eq. (1) places a spatial constraint for the curve evolution. Studies have shown that Chan-Vese model can be implemented by nonlinear diffusion preprocessing followed by K-mean clustering [40]. Second, the hierarchical region-fusion approach emphasizes homogeneity outside the object contour more than inside of it and hence is less affected by blood volume in large vessels, even when the lesion is very small. Fig. 8 shows examples of non-accurate segmentation by our previous methods presented in Ref. [10]. This was due to the presence of large blood vessels that caused smooth transition of color. For comparison, results from this new method are shown in Fig. 6(f).

To compare our NBGP method with GPAC [28], we applied GPAC to XLM and TLM images using the same pre-processing settings and the same initial contour obtained from the Chan-Vese model and region fusion scheme. From Table 2 and Fig. 7, we see that our method gives better results than GPAC in both imaging modalities. For TLM images, our method's error reduction from GPAC is 22.9%. That is

because GPAC uses global information and can be easily misled by blood in large vessels.

For the ELM images, three dermatologists performed lesion segmentation manually to create our reference set. In our experiments, we compared our method with the Chan-Vese model and GPAC, and also studied the variation among manual segmentation results. When comparing with the Chan-Vese model and GPAC, we make sure that all images undergo the same pre-processing procedure and use the same parameters as in our NBGP method.

When comparing with GPAC [28], we only used the first three scales of the pyramid and did not perform curve evolution on the original images. The reason is that GPAC takes a long time to run on some high resolution images, e.g. it takes more than 1 h to perform just one iteration on a  $1322 \times 875$  image. To be fair, we performed the same procedure for NBGP and the ground truth contours were also mapped to the third scale of the pyramid. The comparison result is shown in Fig. 11(c).

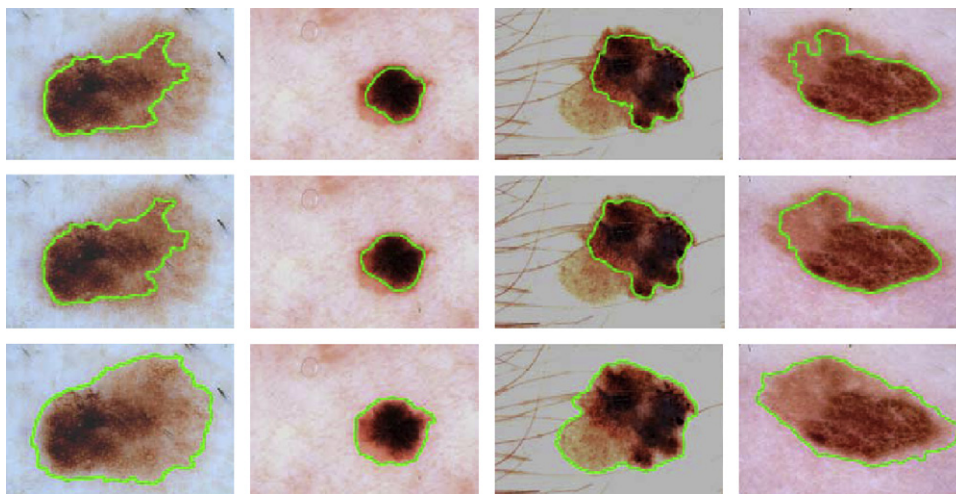
In many cases, the Chan-Vese model and GPAC achieved good results. An example is shown in Fig. 9. For images with asymmetric lesions, however, the Chan-Vese model and GPAC had difficulty in finding all lesion areas, although GPAC performs slightly better than the Chan-Vese model. Fig. 10 provides examples of segmenting asymmetric lesions. The top and middle rows show segmentation contours superimposed on the input images by the Chan-Vese model and GPAC. Because of the imbalanced lesion intensity, both algorithms failed to find the complete region. The failure occurred mostly in the higher intensity part where the lesion is not well-defined. The bottom row illustrates results from our method. The skin lesions were successfully delineated despite the presence of an asymmetric lesion.

Table 3 summarizes the average error ratio of the ELM images from our method, the Chan-Vese model, and manual segmentations. The TRUE segmentation is the average of manual segmentations provided by the dermatologists. Fig. 11(a) shows the comparison of the error ratio distribution for these methods when applied to 100 ELM images.

Table 4 summarizes the average error ratio of the ELM images from our method and GPAC on the resized ELM images. The TRUE



**Fig. 9.** Segmentation results from (a) Chan–Vese model only; (b) GPAC on a resized image; (c) our algorithm.



**Fig. 10.** Segmentation results of asymmetric lesions. Top row: results from Chan–Vese's method. Middle row: results from GPAC on resized images. Bottom row: results from our method. For the skin lesion of the third column, DullRazor method [41] is used for hair removal.

**Table 3**  
ELM images: average segmentation error rate and standard deviation

NBGP	CV	Dermatologists		
4.88% ( $\pm 3.2\%$ )	17.69% ( $\pm 7.4\%$ )	4.45% ( $\pm 3.2\%$ )	2.28% ( $\pm 1.1\%$ )	2.01% ( $\pm 0.8\%$ )

segmentation is created by mapping the average of manual segmentation onto the third level of the Gaussian pyramid. Fig. 11(c) shows the comparison between NBGP and GPAC of the error ratio distribution for the 100 ELM images.

To compare the variability among dermatologists and our NBGP algorithm, we show the average similarity measures for all 100 ELM images in Table 5 and Fig. 11(b), using Eq. (27).

The error ratio of the comparison in Fig. 11(b) and similarity measure in Table 5 show that the performance of our algorithm is very close to the performance of domain experts and both performances are consistent with respect to the ground TRUTH.

## 6. Discussion and conclusions

### 6.1. Discussion

In our experiments, we observed that active contours were attracted by structures on healthy skin or noise near the boundary. This is because the band size ( $eb_s$  in Algorithm 2) used to compute the energy function is very small (since we chose a small  $eb_s$  for the level set function update to reduce computational cost) compared to the dimension of the image, and thus the method is almost an edge based scheme. We mitigated the effect of edge leaking by using the multiscale approach.

Our method exhibits advantages over the traditional edge-based schemes. Unlike edge-based active contours, such as geodesic active contours and Gradient Vector Flow (GVF) snakes, which rely only on gradient information, our NBGP uses local region information. As shown in Fig. 12, the GVF snake was attracted by strong false edges, and the curve evolution stopped before the real boundary was reached. Fig. 12(a) is the curve obtained from the Chan–Vese model and served as the initial curve for GVF snake and NBGP. Fig. 12(b) is the curve obtained from GVF snake after 100 iterations. We can see that the GVF snakes were attracted by strong false edges inside the lesion and moved away from the boundary. On the other hand, contours obtained from NBGP after 100 iterations (see Fig. 12(c)) were moving toward the lesion boundary. Quantitatively, compared to the segmentation from the Chan–Vese model, our NBGP method showed improvements of 48.9% and 58.2% (with error rate difference of 8% and 10%) in these two images, respectively. In contrast, the error ratio of the GVF segmentation method was 24.81% and 29.56% above the Chan–Vese model for both images (with error rate difference of 3.86% and 4.81%).

To reduce the computation cost, Sumengen [28] computed all  $M^2N^2/2$  pairs of dissimilarity measures for an  $M \times N$  image before applying any active contour curve evolution. To store these values, a huge storage space was required. A down-sampling method in the spatial domain has been proposed [28] to reduce the storage complexity. However, it was reported that incorrect boundaries were identified. In many practical cases, down-sampling may not yield satisfactory efficiency improvement. For example, in order to store all these pre-computed similarity measures of pixel pairs for a skin lesion with size  $2465 \times 1637$ , using down-sampling of every 15 pixels in both directions, we still need  $2465^2 \times 1637^2 / 15^2 / 2$  bytes, which

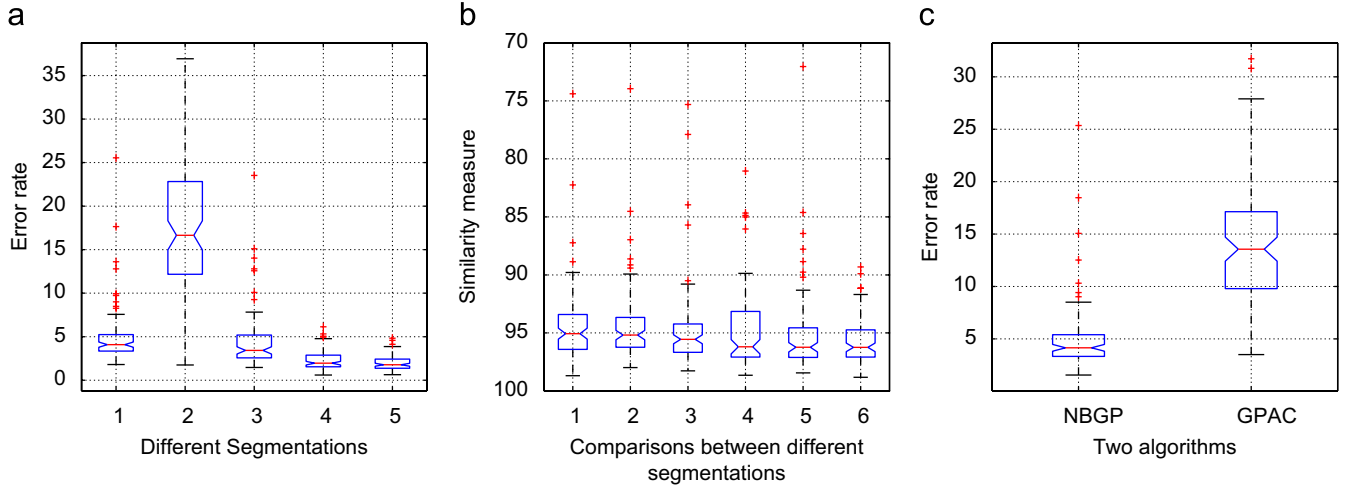


**Fig. 11.** (a) Segmentation error ratio. The labels on the x-axis are: 1. GPNB; 2. Chan-Vese; 3–5 are three dermatologists. (b) Error ratio between our method and manual results. The labels on the x-axis are: 1–3, our method vs. manual results. 4–6, inter-dermatologists variation. (c) Segmentation error ratio on resized images of NBGP and GPAC.

**Table 4**  
Resized ELM images: average segmentation error rate and standard deviation

NBGP	GPAC
5.02% ( $\pm 3.3\%$ )	14.07% ( $\pm 6.0\%$ )

**Table 5**  
Average similarity measure and standard deviation for ELM images

NBGP–Dr. G	NBGP–Dr. S	NBGP–Dr. M	Dr. G–Dr. S	Dr. G–Dr. M	Dr. S–Dr. M
94.44% ( $\pm 3.2\%$ )	94.40% ( $\pm 3.2\%$ )	94.79% ( $\pm 3.5\%$ )	94.86% ( $\pm 3.3\%$ )	95.27% ( $\pm 3.4\%$ )	95.75% ( $\pm 1.9\%$ )

NBGP–Dr. G means the similarity measure between result of NBGP and manual segmentation of Dr. G. Similar notations are used for other columns as well.

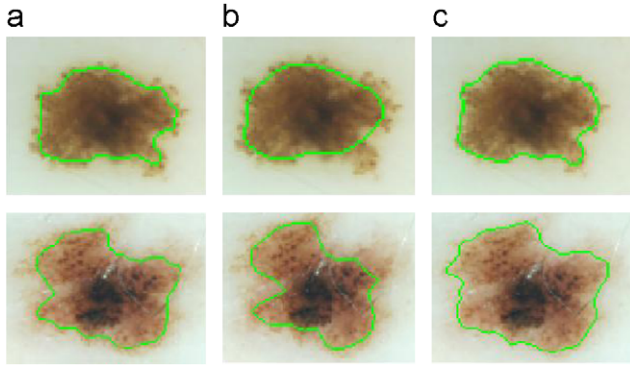


**Fig. 12.** Segmentation results comparison among different active contours: (a) region-based (Chan-Vese), (b) edge-based (GVF) (c) our method (NBGP).

is approximately 32 GB of memory (assume one byte is used for every pixel). Hence, in our algorithm, precomputing is not used and the storage complexity of our algorithm is  $O(N^2)$  for an image with dimension  $N \times N$ . Even without precomputing, the execution time of our method is still descent because we reduce the time complexity from  $O(N^3)$  in Ref. [28] to  $O(N^2)$  in each iteration, and only a simple intensity feature is used.

In addition, as discussed in Ref. [42], by choosing different values for the weighting parameter  $\lambda_k$ , the Chan-Vese model can also handle asymmetric structures. However, there is no

computationally efficient way for automatic parameter selection. In this paper, we showed that NBGP active contour can handle the asymmetric structures robustly with respect to the weighted parameters.

## 6.2. Conclusions

Segmentation of a skin lesion is an important step in automatic computer-based melanoma detection systems. Active contours are widely used for general image segmentation, and edge-based active contours, such as GVF [16,17], have been applied to skin lesion segmentation with descent results. In this paper, we developed a novel hierarchical region-fusion-based segmentation framework that employs a computationally efficient curve evolution method that is based on narrow band energy. We formulated and derived the solution for a generalized energy function of the narrow band curve evolution problem. We then applied the new framework (Algorithms 1 and 2) and the standard Chan-Vese, GPAC [28], and our narrow band graph partitioning (NBGP) method to skin lesion images acquired under three imaging modalities (ELM, XLM, and TLM). Our results showed that the new region-based active contours outperform our previous thresholding and clustering-based methods [10] as well as edge-based method (GVF). Using local features, the new NBGP curve evolution scheme was able to produce the best segmentation results and achieve accuracy very close to manual segmentation by specialists. It exhibited great robustness even for lesions with weak and/or false edges, highly asymmetric lesions, dense hair or bubble artifacts, and presence of noise.

Within the active contours, we only used the intensity feature of each pixel within the image. An obvious extension is to incorporate color and texture features, either independently, or combine them within the same objective function, i.e., in the (dis)similarity measure. A generic framework that incorporates different forms of information (region and edge) of different nature (intensity, color, texture, and shape) and can perform lesion segmentation efficiently for different imaging modalities is the future direction of our work.

## Acknowledgments

The authors are grateful to Dr. William Stoeker, M.D. and Nizar Mullani for providing the ELM, XLM and TLM images and clinical expertise.



## References

- [1] Anonymous, Cancer Facts and Figures 2002, 2002.
- [2] H. Ganster, A. Pinz, R. Rohrer, E. Wildling, M. Binder, H. Kittler, Automated melanoma recognition, *IEEE Trans. Med. Imaging* 23 (6) (2001) 233–239.
- [3] S. Menzies, L. Bischof, M.B.E.H. Talbot, A. Gutenev, M. Avramidis, L. Wong, S.K. Lo, G. Mackellar, V. Skladnev, W. McCarthy, J. Kelly, B. Cranney, P. Lye, H. Rabinovitz, M. Oliviero, A. Blum, A. Virol, B. Dembrosi, R. McCleod, H. Koga, C. Grin, R. Braun, R. Johr, The performance of solarscan: an automated dermoscopy image analysis instrument for the diagnosis of primary melanoma, *Arch. Dermatol.* 141 (2005) 1388–1396.
- [4] M. Moncrieff, S. Cotton, E. Claridges, P. Hall, Spectrophotometric intracutaneous analyses: a new technique for imaging pigmented skin lesions, *Br. J. Dermatol.* 146 (2002) 448–457.
- [5] M. Elbaum, A. Kopf, H. Rabinovitz, R. Langley, H. Kamino, M.M. J. et al., Automatic differentiation of melanoma from melanocytic nevi with multispectral digital dermoscopy: a feasibility study, *J. Am. Acad. Dermatol.* 44 (2001) 207–218.
- [6] G. Betta, G. Leo, G. Fabbrocini, A. Paolillo, M. Scalvenzi, Automatic application of the '7-point checklist' diagnosis method for skin lesions: estimation of chromatic and shape parameters, in: *Proceedings of the IEEE Instrumentation and Measurement Technology Conference (IMTC05)*, vol. 3, May 2005, pp. 1818–1822.
- [7] R. Jailani, H. Hashim, M.N. Taib, S. Sulaiman, Border segmentation on digitized psoriasis skin lesion images, in: 2004 IEEE Region 10 Conference TENCON, November 2004, pp. 596–599.
- [8] E. Maglogiannis, C. Caroni, S. Pavlopoulos, V. Karioti, Utilizing artificial intelligence for the characterization of dermatological ages, in: *NNESMED*, 2001, pp. 362–368.
- [9] K. Taouil, N.B. Romdhane, Automatic segmentation and classification of skin lesion images, in: *The 2nd International Conferences on Distributed Frameworks for Multimedia Applications*, May 2006, pp. 1–12.
- [10] G. Zouridakis, M. Doshi, N. Mullani, Early diagnosis of skin cancer based on segmentation and measurement of vascularization and pigmentation in nevoscope images, in: *Proceedings of the 26th Annual International Conference of the IEEE EMBS*, IEEE, 2004, pp. 1596–1593.
- [11] M.E. Celebi, Y.A. Aslandogan, P.R. Bergstresser, Unsupervised border detection of skin lesion images, in: *ITCC (2)*, IEEE Computer Society, 2005, pp. 123–128.
- [12] M.E. Celebi, Y.A. Aslandogan, P.R. Bergstresser, Mining biomedical images with density-based clustering, in: *ITCC (1)*, IEEE Computer Society, 2005, pp. 163–168.
- [13] M. Kass, A. Witkin, D. Terzopolous, Snakes: active contour models, *Int. J. Comput. Vision* 1 (4) (1988) 321–331.
- [14] C. Xu, J.L. Prince, Snakes, shapes, and gradient vector flow, *IEEE Trans. Image Process.* 7 (3) (1998) 359–369.
- [15] V. Caselles, R. Kimmel, G. Sapiro, Geodesic active contours, in: *ICCV*, 1995, pp. 694–699.
- [16] D.H. Chung, G. Sapiro, Segmenting skin lesions with partial-differential-equations-based image processing algorithms, *IEEE Trans. Med. Imaging* 19 (7) (2000) 763–767.
- [17] B. Erkol, R. Moss, R. Stanley, W. Stoecker, E. Hvatum, Automatic lesion boundary detection in dermoscopy images using gradient vector flow snakes, *Skin Res. Technol.* 11 (2005) 17–26.
- [18] T.F. Chan, L.A. Vese, Active contours without edges, *IEEE Trans. Image Process.* 10 (2) (2001) 266–277.
- [19] A. Tsai, A.J. Yezzi, A. Willsky, Curve evolution implementation of the mummford-shah functional for image segmentation, denoising, interpolation, and magnification, *IEEE Trans. Image Process.* 10 (8) (2001) 1169–1186.
- [20] X. Yuan, J. Zhang, X. Yuan, B.P. Buckles, Multi-scale feature identification using evolution strategies, *Image Vision Comput.* J. 23 (6) (2005) 555–563.
- [21] X. Yuan, Z. Yang, G. Zouridakis, N. Mullani, Svm-based texture classification and application to early melanoma detection, in: *IEEE EMBS*, 2006, pp. 4775–4778.
- [22] X. Yuan, J. Zhang, B.P. Buckles, Evolution strategies based image registration via feature matching, *Information Fusion* 5 (4) (2004) 269–282.
- [23] H. Pehamberger, A. Steiner, K. Wolff, In vivo epiluminescence microscopy of pigmented skin lesions. I. Pattern analysis of pigmented skin lesions, *J. Am. Acad. Dermatol.* 17 (4) (1987) 571–583.
- [24] K. Wolff, M. Binder, H. Pehamberger, Epiluminescence microscopy: a new approach to the early detection of melanoma, *Adv. Dermatol.* 9 (1) (1994) 45–56.
- [25] M. Binder, Skin examination device, US Patent Number 6,032,071, Published in 2000.
- [26] N. Mullani, R. Talpur, N. Apisarnthanarax, M. Weinstock, R. Drugge, C. Ahn, V. Prieto, M. Duvic, Side-transillumination epiluminescence imaging for diagnosis of dysplastic nevi and melanoma a comparison to oil and cross-polarization epiluminescence imaging, in press.
- [27] S. Osher, J. Sethian, Fronts propagating with curvature dependent speed: algorithms based on Hamilton Jacobi formulations, *J. Comput. Phys.* 79 (1988) 12–49.
- [28] B. Sumengen, B.S. Manjunath, Graph partitioning active contours (GPAC) for image segmentation, *IEEE Trans. Pattern Anal. Mach. Intell.* 28 (4) (2006) 509–521.
- [29] J. Mille, R. Bone, P. Makris, H. Cardot, 2D and 3D deformable models with narrowband region energy, in: *International Conference on Image Processing*, 2007, pp. II: 57–60.
- [30] B. Song, T. Chan, Fast algorithm for level set based optimization, 2002.
- [31] D. Chop, Computing minimal surfaces via level set curvature flow, *J. Comput. Phys.* 106 (1) (1993) 77–91.
- [32] D. Adalsteinsson, J. Sethian, A fast level set method for propagating interfaces, *J. Comput. Phys.* 3 (118) (1995) 269–277.
- [33] N. Paragios, R. Deriche, Geodesic active contours and level sets for the detection and tracking of moving objects, *IEEE Trans. Pattern Anal. Mach. Intell.* 22 (3) (2000) 266–280.
- [34] E. Adelson, C. Anderson, J. Bergen, P. Burt, J. Ogden, Pyramid methods in image processing, *RCA Engineer* 29 (6) (1984) 33–41.
- [35] Nevoscope web site at ([www.nevoscope.com](http://www.nevoscope.com)).
- [36] P. Dhawan, Apparatus and method for skin lesion examination, US Patent Number 5,146,923, Published in 1992.
- [37] M.E. Celebi, Y.A. Aslandogan, P.R. Bergstresser, Mining biomedical images with density-based clustering, in: *International Conference on Information Technology: Coding and Computing*, ITCC 2005, Proceedings, IEEE, 2005, pp. 163–168.
- [38] M.E. Celebi, Y.A. Aslandogan, P.R. Bergstresser, Unsupervised border detection of skin lesion images, in: *International Conference on Information Technology: Coding and Computing*, ITCC 2005, Proceedings, IEEE, 2005, pp. 123–128.
- [39] C. Pluempitiririyawej, J.M.F. Moura, Y.-J.L. Wu, C. Ho, STACS: new active contour scheme for cardiac MR image segmentation, *IEEE Trans. Med. Imaging* 24 (5) (2005) 593–603.
- [40] F. Gibou, R. Fedkiw, A fast hybrid k-means level set algorithm for segmentation (July 17 2002).
- [41] T. Lee, V. Ng, R. Gallagher, A. Coldman, D. Mclean, Dullrazor: a software approach to hair removal from images, *Comput. Biol. Med.* 27 (6) (1997) 533–543.
- [42] S. Gao, T.D. Bui, Image segmentation and selective smoothing by using mummford-shah model, *IEEE Trans. Image Process.* 14 (10) (2005) 1537–1549.

**About the Author**—XIAOJING YUAN received B.S. in electrical engineering from Hefei University of Technology in China in 1994, followed by a M.S. in computer engineering from University of Science and Technology of China in 1997 and another M.S. degree computer science in 2001 and a Ph.D. degree in Intelligent Systems in 2003, both from Tulane University. She joined the Engineering Technology Department of the University of Houston in 2004, where she has been actively involved in research areas such as biomedical imaging analysis, data mining, pattern recognition, and information technology in biomedical applications. She founded and served as director for “Intelligent Sensor Grid and Informatics Lab” in 2005. She has years’ experience in embedding intelligence into sensors and actuators to deal with uncertainties. She authored and co-authored more than 40 technical papers; has one patent and another one filed in 2008. She has been very active in professional organization such as IEEE and ISA; being reviewer for top-rank journals and conferences, and chairing and co-chairing conference sessions in “intelligent sensor network”.

**About the Author**—NING SITU received a B.S. degree in Computer Science from Sun Yat-sen University in 2006. He has been a Ph.D. student at the Computer Science Department, University of Houston since 2006. His current research interests include pattern recognition, image segmentation, and statistical imaging analysis for cancer detection.

**About the Author**—GEORGE ZOURIDAKIS received a Dr.Ing. degree in Electronics Engineering from the University of Rome “La Sapienza” in 1987, followed by an M.S. in Biomedical Engineering in 1990 and a Ph.D. in Electrical Engineering in 1994, both from the University of Houston. He has been on the faculty of The University of Texas-Houston Medical School from 1994 to 2001, where his clinical activities included Intraoperative Monitoring, Functional Brain Mapping, and Deep Brain Stimulation. He joined the University of Houston in 2001 and he is the Director of the Biomedical Imaging Lab. His current research interests are in the areas of Biomedical Imaging, Computational Biomedicine, Functional Brain Mapping, and Biosignal Analysis and Modeling. He is the main author of a book on Intraoperative Monitoring, CRC Press, 2001, and the Co-Editor-in-Chief of the “Handbook of Biomedical Technology and Devices”, CRC Press, 2003. He has developed courses, given lectures, organized sessions at national and international conferences on Medical Imaging and Brain Mapping, and has published more than 160 referred papers and abstracts. He is an Associate Editor of the IEEE Transactions on Biomedical Engineering, the Chair of the IEEE EMBS Houston Chapter, and he is also listed on Who’s Who in America.